1   **Modelling dynamic changes in blood flow and volume in the cerebral vasculature**

2   SJ Payne* and WK El-Bouri

3   Institute of Biomedical Engineering, Department of Engineering Science, University of Oxford

4   Parks Road, Oxford OX1 3PJ, UK

5   stephen.payne@eng.ox.ac.uk; wahbi.el-bouri@eng.ox.ac.uk

6   *Corresponding author

7

12

13   **Abstract**

14   The cerebral microvasculature plays a key role in the transport of blood and the delivery of nutrients

15   to the cells that perform brain function. Although recent advances in experimental imaging

16   techniques mean that its structure and function can be interrogated to very small length scales,

17   allowing individual vessels to be mapped to a fraction of 1 μm, these techniques currently remain

18   confined to animal models. In-vivo human data can only be obtained at a much coarser length scale,

19   of order 1 mm, meaning that mathematical models of the microvasculature play a key role in

20   interpreting flow and metabolism data. However, there are close to 10,000 vessels even within a

21   single voxel of size 1 mm^3. Given the number of vessels present within a typical voxel and the

22   complexity of the governing equations for flow and volume changes, it is computationally

23   challenging to solve these in full, particularly when considering dynamic changes, such as those

24   found in response to neural activation.

25   We thus consider here the governing equations and some of the simplifications that have been

26   proposed in order more rigorously to justify in what generations of blood vessels these

27   approximations are valid. We show that two approximations (neglecting the advection term and

28   assuming a quasi-steady state solution for blood volume) can be applied throughout the cerebral

29   vasculature and that two further approximations (a simple first order differential relationship

30   between inlet and outlet flows and inlet and outlet pressures, and matching of static pressure at

31   nodes) can be applied in vessels smaller than approximately 1 mm in diameter. We then show how

32   these results can be applied in solving flow fields within cerebral vascular networks providing a

33   simplified yet rigorous approach to solving dynamic flow fields and compare the results to those

34   obtained with alternative approaches. We thus provide a framework to model cerebral blood flow

35   and volume within the cerebral vasculature that can be used, particularly at sub human imaging

36   length scales, to provide greater insight into the behaviour of blood flow and volume in the cerebral

37   vasculature.

38   **1 Introduction**

39   Since 2006 there has been a great deal of interest in models of the cerebral microcirculation. This

40   has been driven by the recent ability to obtain experimental data about microvascular networks,

41   both in humans and in animal models. The former has mainly been based on the collection of post-

42   mortem casts obtained by Duvernoy et al. (1981), and these experimental data have been presented

43   in detail by Cassot et al. (2006), Lauwers et al. (2008) and Lorthois et al. (2011). Casts of animal

44   microvascular networks have also been extracted and the flow in them modelled, see for example

45   Fang et al. (2008), Weber et al. (2008), Reichold et al. (2009), Tsai et al. (2009), Guibert et al. (2010),

46   Blinder et al. (2010), Safaeian et al. (2011), Kasische et al. (2011), Linninger et al. (2013), Gagnon et

47   al. (2015), Gould et al. (2017) and Schmid et al. (2017). Many of the models listed above have also

48   examined the transport of oxygen and the coupling between this and cerebral blood flow.

49   Although there has been a great deal of progress on robustly extracting vascular networks from

50   imaging data and converting them into accurately segmented three-dimensional networks, see for

51   example Gould et al. (2017), acquiring large volumes of such data remains a time-consuming and

52   expensive task that can only be undertaken with considerable expertise. The strong dependence of

53   vessel resistance on vessel radius means that accurate values of the vessel diameter are critical if the

54   flow field is to be calculated accurately. The strong dependence of the chosen boundary conditions

55   on the flow simulations has also been noted by many authors, for example Lorthois et al. (2011).

56   These factors, together with the high vessel density that means that solving the flow field in volumes

57   of tissue that are of the length scale of a human imaging voxel (of order 1 mm) is highly

58   computationally challenging, has driven the development of homogenisation techniques based on

59   the creation of artificial networks that match experimentally measured properties, Su et al. (2012),

60   El-Bouri and Payne (2015) and El-Bouri and Payne (2016), and coupling these with models over

61   multiple length scales, El-Bouri and Payne (2018). These techniques enable a scaling up of networks

62   to a voxel scale and hence the flow fields can be related to imaging data, most easily through the use

63   of transit time distributions, see for example Park and Payne (2013). Other authors have developed

64   vascular networks through the use of bifurcating vessels, for example Boas et al. (2008) and Payne

65   and Lucas (2017), although in these models no spatial information is considered.

66   At a voxel level, the vasculature comprises vessels over a relatively wide range of length scales, with

67   diameters ranging from a few micrometres to hundreds of micrometres. Consideration does thus

68   need to be given to the assumptions and choice of equations that govern blood flow over these

69   length scales, in particular when attempting to bridge the 'imaging gap', when the assumptions valid

70   in the large vessels and those in the microvasculature may be significantly different. At the smallest

71   length scales, nearly all authors use the Poiseuille equation in some form, with viscosity either taken

72 to be constant, based on vessel diameter or based on vessel diameter and haematocrit, as shown in

73 Table 1. In the latter two cases, empirical relationships are normally used, with a variety of different

74 relationships having been applied. Once the resistance to flow is known, then the network reduces

75 to a conductance matrix, which can be solved numerically, either by simple inversion for networks

76 with constant haematocrit or by iteration for networks with non-constant haematocrit. It is usually

77 assumed that at small length scales static pressure is conserved at nodes, as has been done in all the

78 studies listed thus far.

79 Most of the models listed in Table 1 assume steady state flow conditions, with only a few

80 considering the dynamic response, although this plays an important part in interpreting the

81 response to changes in neural activity. Only the models by Boas et al. (2008), Reichold et al. (2009),

82 Gagnon et al. (2015) and Payne and Lucas (2017) consider the dynamic response of the small vessels

83 in the cerebral vasculature. These mostly assume a non-linear compliance of the vessels, enabling

84 changes in flow to drive changes in volume. Such changes in blood volume are of particular

85 importance in the context of imaging techniques such as the BOLD response, where short-term

86 changes in blood volume can strongly influence the response.

Model	Static/dynamic	Flow model	Viscosity model
Fang et al. (2008)	Static	Poiseuille equation	Constant
Boas et al. (2008)	Dynamic	Poiseuille equation and non-linear compliance	Pries et al. (1992), with haematocrit as function of diameter
Reichold et al. (2009)	Dynamic	Poiseuille equation and non-linear compliance	Pries et al. (1992), with haematocrit as function of diameter
Guibert et al.	Static	Poiseuille equation	Kiani and Hudetz (1991) or Pries

(2010)			and Secomb (2005), with haematocrit model
Lorthois et al. (2011)	Static	Poiseuille equation	Pries et al. (1996), with haematocrit model
Safaeian et al. (2011)	Static	Poiseuille equation	Pries and Secomb (2005), with haematocrit model
Linninger et al. (2013)	Static	Poiseuille equation	Pries et al. (1996), with constant haematocrit
Gagnon et al. (2015)	Dynamic	Poiseuille equation and non-linear compliance	Pries et al. (1990), 'corrected for haematocrit'
Gould et al. (2017)	Static	Coupled model of flow and haematocrit, rigid vessels	Plasma skimming model
Schmid et al. (2017)	Static	Poiseuille equation	Pries et al. (1992), with tracking of red blood cells
Payne and Lucas (2017)	Dynamic	Poiseuille equation	Pries et al. (1992), with constant haematocrit
El-Bouri and Payne (2018)	Static	Poiseuille equation	Pries et al. (1992), with constant haematocrit

87 **Table 1** Summary of network models of cerebral blood flow and assumptions used

88 Other approaches have taken a more 'top-down' methodology, where lumped parameter models

89 (e.g. windkessel models) are used, with the lumped parameters aiming to capture the overall

90 behaviour of flow through large numbers of vessels in a very small number of parameters, see for

91 example those used by Ress et al. (2009), Kim et al. (2013) in the context of models of oxygen

92 delivery, and Buxton et al. (1998) and many subsequent studies (for example Aquino et al. (2014)) in

93 the context of models of the BOLD response. Such models have a valuable role to play in

94   understanding the behaviour at large scales, but are inevitably limited by both their simplicity and

95   the difficulties involved in linking the model parameters to the underlying network physiology.

96   The assumptions made are often very different in models of flow in the larger vessels, for example

97   when the dynamic behaviour of the flow field plays an important part in both flow and volume, and

98   when total pressure is often conserved at nodes, see for example Alastruey et al. (2007). In order to

99   link models across the 'imaging gap', care has to be taken and the limits of assumptions fully

100   understood. For a comprehensive review of models of cerebral blood flow, the reader is referred to

101   Payne (2017).

102   In this paper we thus consider the modelling of cerebral blood flow and volume in networks of blood

103   vessels in detail, justify suitable approximations that can be made, and propose a framework that

104   can be used that is mathematically rigorous and computationally simple. We will also consider the

105   limits of the approximations and hence illustrate how models can be developed that will cover

106   multiple scales. In order to do this, we consider the governing equations and use these to develop a

107   model relating blood flow and volume to pressure in a single vessel; finally we link vessels together

108   within a network and then show how the equations can be solved dynamically within a network. In

109   the last section we will consider each of these in turn before illustrating our proposed approach in

110   the context of the cerebral vasculature, comparing simulation results with those obtained using

111   previous approaches.

112   **2 Theory**

113   We assume blood to be a Newtonian fluid of viscosity μ and density ρ in a flow field that is governed

114   by the incompressible form of the Navier-Stokes equations. These fundamental fluid flow equations

115   are based on the concepts of conservation of mass and balance of forces; a full explanation and

116   derivation can be found in many sources, see for example Acheson (1990). Hence:

117
$$\frac{\partial \mathbf{u}}{\partial t} + (\mathbf{u}.\nabla)\mathbf{u} = -\frac{1}{\rho}\nabla p + \frac{\mu}{\rho}\nabla^2 \mathbf{u} \ (1)$$

118   with velocity field **u** driven by a pressure field p. In an axisymmetric vessel this reduces to:

119
$$\frac{\partial u}{\partial t} + u\frac{\partial u}{\partial x} = -\frac{1}{\rho}\frac{\partial p}{\partial x} + \frac{\mu}{\rho}\nabla^2 u \ (2)$$

120   where the flow velocity has only an axial component, u, which is a function of radius, r, axial position,

121   x, and time, t. In this latter case, the pressure gradient can be shown to be only a function of axial

122   position and time, i.e. the pressure is uniform over the cross-sectional area, based on order of

123   magnitude arguments, Canic and Kim (2003). A similar order of magnitude argument can be used to

124   neglect the radial component of the velocity field when the variations in the vessel cross-section are

125   not too fast, Canic and Kim (2003). We note that the assumption of a Newtonian fluid is a limitation

126   to this analysis, but one that we will consider more fully in the Discussion. For ease of reference,

127   schematics of the different components of the model are shown in Figure 1, to which we refer

128   throughout.

129
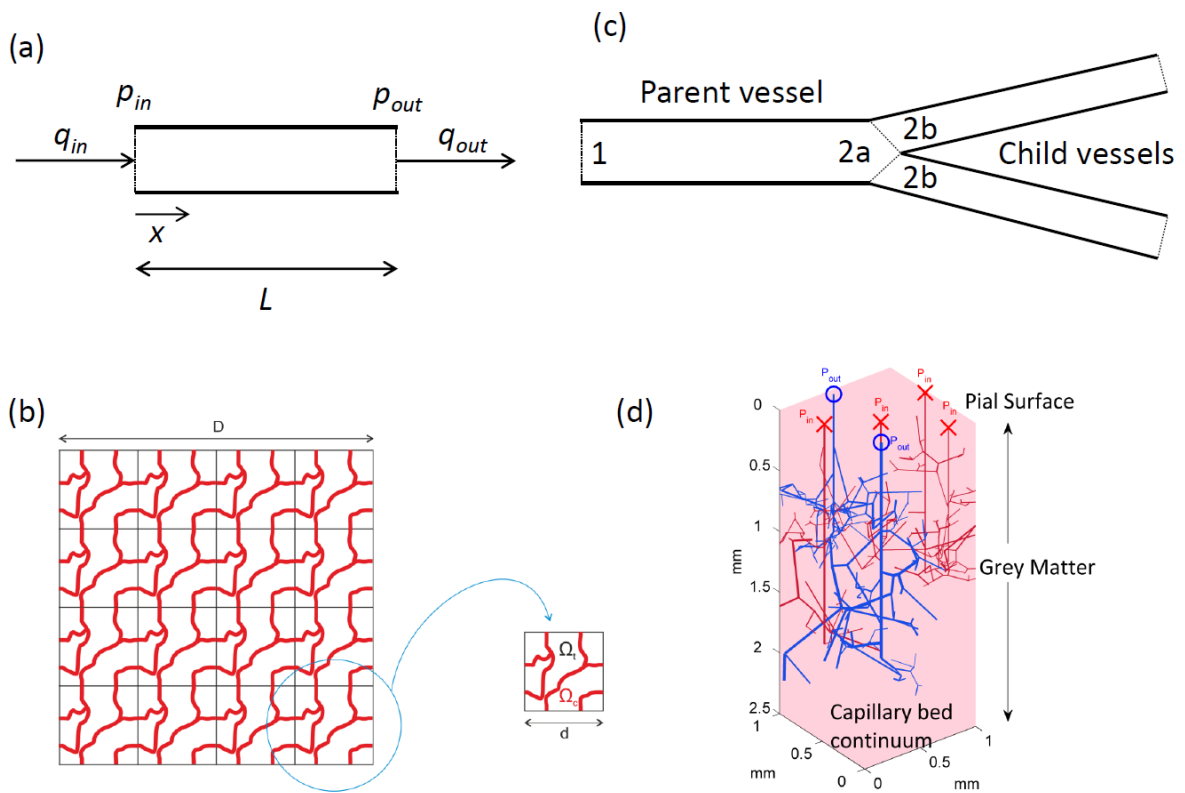
Figure 1 Schematic of components of model: (a) single vessel model; (b) continuum model; (c) node

131   model; (d) coupled penetrating vessel and capillary bed continuum model. Figures (b) and (d)

132   reproduced from El-Bouri (2017)

2.1 Result 1: The advection term can be neglected when $\frac{E}{\rho U^2}\frac{h}{R} \gg \frac{3}{2}$ (E is Young's modulus, ρ is fluid density, U is flow velocity, h is wall thickness and R is vessel inner radius)

135   The first result that we show is that the advection term can be neglected in models of cerebral blood

136   flow when the vessel wall stiffness scaled by wall thickness to radius ratio is greater than a multiple

137   of the dynamic head. This result is required first to enable us to write down the governing equations

138   in a simplified form so that we can derive a model for the inlet and outlet flows in the next section.

139   We will demonstrate this in two parts. We first consider the flow in individual vessels, Figure 1a,

140   since a simple result can be obtained, before considering the flow field across multiple scales, Figure

141   1b. This latter approach allows us to consider the flow field as a whole; this is valuable since it links

142   to previous work that has shown how the flow field in the capillary vessels can be modelled using

143   homogenisation, El-Bouri and Payne (2015). For simplicity we only consider the steady state solution,

144   but this does not affect the result.

Single vessels

146   We firstly reduce the steady state form of Equation 2 to non-dimensional form, where we reference

147   velocity and pressure to characteristic values, U and P respectively:

$$u^*\frac{\partial u^*}{\partial x^*} = -\left(\frac{P}{\rho U^2}\right)\frac{\partial p^*}{\partial x^*} + \frac{1}{Re_L}\nabla^2 u^* \quad (3)$$

149   where the star is used here to denote a value as a fraction of its characteristic value, i.e. $u^* = u/U$,

150     $p^* = p/P$ and $x^* = x/L$, and noting that we do not assume any relationship between characteristic

151   pressure and characteristic velocity, retaining generality at this stage. The co-ordinate x is

152   referenced to vessel length, L (and hence the ∇^2 operator is also made non-dimensional with respect

153   to L). Note that Reynolds number in Equation 3 is based on vessel length:

154
$$Re_L = \frac{\rho U L}{\mu} \text{ (4)}$$

155   We use a subscript for Reynolds number throughout to make it clear what length scale is being used.

156   The aim is then to consider the relative magnitudes of the advection and pressure gradient terms,

157   since these are the two terms with first order axial derivative terms and thus terms that can be

158   compared directly through order of magnitude arguments.

159   Conservation of mass, averaged over the cross-sectional area, gives:

160
$$\frac{\partial A}{\partial t} + \frac{\partial q}{\partial x} = 0 \text{ (5)}$$

161   where the flow rate, q, is the integral of the axial velocity over the cross-sectional area: see Canic

162   and Kim (2003) for a formal derivation of this result. In the steady state this reduces to a flow rate

163   that is invariant over axial length, as expected. Hence:

164
$$A = \frac{q}{\overline{U}} \text{ (6)}$$

165   where the area-averaged velocity is given by $\overline{U}$ (which can vary along the vessel). We next assume

166   that a relationship can be formulated between steady state pressure and cross-sectional area

167   (without at this stage specifying its form), i.e. $p = p(A)$. We neglect any viscous component of the

168   wall response here as we are only considering the steady state behaviour: note, however, that we

169   retain the viscous behaviour of the fluid, which means that the pressure will drop in the direction of

170   flow and hence the cross-sectional area of the vessel will also change in order to maintain flow rate.

171   We also neglect any axial stiffness, only considering the radial stiffness, as is commonly done, for

172   simplicity.

173   Using this assumption, Equations 3 and 6 yields:

9

174
$$u^* \frac{\partial u^*}{\partial x^*} = \left[A \frac{dp}{dA} \left(\frac{1}{\rho U^2} \right) \frac{U}{\overline{U}} \right] \frac{\partial \overline{U}^*}{\partial x^*} + \frac{1}{Re_R(R/L)} \nabla^2 u^* \quad (7)$$

175   where Reynolds number in Equation 7 is now based on vessel radius and this is scaled by the ratio of

176   vessel radius to length (R/L). The key parameter is then the square bracket, since if this is much

177   larger than 1, the advection term can be neglected in comparison with the pressure gradient term

178   (note that although the derivatives are of different velocity terms, one being velocity as a function of

179   radius and one the area-averaged velocity, they are of the same order of magnitude).

180   We therefore need to consider the pressure-area relationship more closely. Many different forms

181   have been proposed for this, for example those by Langewouters et al. (1984), Stergiopoulos et al.

182   (1992) and Formaggia et al. (1999). For simplicity we use the relationship that results from assuming

183   static radial equilibrium of an isotropic elastic material with Young's modulus E, Poisson ratio

184   v,reference wall thickness h_{ref} and radius R_{ref}, as quoted by Formaggia et al. (1999) and widely

185   used elsewhere:

186
$$p - p_{ref} = \frac{E h_{ref}}{R_{ref}(1 - v^2)} \left(\sqrt{\frac{A}{A_{ref}}} - 1 \right) \quad (8)$$

187   where the wall stiffness relates changes in pressure relative to a reference value, p_{ref}, to changes in

188   cross-sectional area relative to a reference value, $A_{ref} = \pi R_{ref}^2$. Note that this model assumes that

189   there is no axial stiffness: the wall thus responds at each axial location to the pressure at that

190   location without reference to the remainder of the pressure field. More sophisticated models have

191   been used, see for example Pedrizzetti and Perktold (2003), but this assumption is very commonly

192   made in models of blood flow and is sufficient for the order of magnitude argument being made

193   here.

194   This then gives:

195
$$\left[A\frac{dp}{dA}\left(\frac{1}{\rho U^2}\right)\frac{U}{\overline{U}}\right] = \frac{1}{2}\frac{E}{\rho U^2}\frac{h_{ref}}{R_{ref}(1-\nu^2)}\sqrt{\frac{A}{A_{ref}}}\frac{U}{\overline{U}} \quad (9)$$

196   Since we can select the characteristic velocity to be close to the area-averaged value and assuming

197   that all values are close to their reference value, this simplifies to give:

198
$$\left[A\frac{dp}{dA}\left(\frac{1}{\rho U^2}\right)\frac{U}{\overline{U}}\right] \approx \frac{2}{3}\frac{E}{\rho U^2}\frac{h}{R} \quad (10)$$

199   where we also assume a value of Poisson ratio of 0.5, denoting an incompressible material, as is

200   commonly done. For advection to be neglected, this term must be significantly greater than 1, hence

201    $\frac{E}{\rho U^2}\frac{h}{R} \gg \frac{3}{2}$. We will examine this result again in the context of the cerebral vasculature later.

202   Note that although we have only considered the steady state response here, the result is also valid

203   for dynamic flow fields, since we have compared the two terms with first order axial derivatives and

204   thus including dynamic terms in the equations will not affect the validity of this particular result. It

205   would be worth considering in future the relative magnitudes of the acceleration term and the

206   viscous wall behaviour (the two terms with first order time derivatives). It should be noted, however,

207   that the available data for visco-elastic models of the vessel wall in the cerebral vasculature are very

208   sparse.

209   **Continuous flow field**

210   Having considered the flow in individual vessels above, we next show how the advection term can be

211   neglected when considering the flow field as a continuous one. This approach is based on the

212   method set out by Shipley and Chapman (2010) and previously adapted for the cerebral

213   microcirculation by El-Bouri and Payne (2015). We include this analysis since we have previously

214   shown how the flow field within volumes of brain tissue can be modelled using a coupled approach

215   that incorporates both the flow in individual non-capillary vessels and a Darcy flow for the capillary

216   vessels, El-Bouri and Payne (2018), and thus wish to show that the advection term can be neglected

217   when considering the flow field as a continuum.

218   As before, we consider the solution in the steady state but start from the Navier-Stokes equations

219   for incompressible flow:

220
$$(\mathbf{u}_c.\nabla)\mathbf{u}_c = -\frac{1}{\rho}\nabla p_c + \frac{\mu}{\rho}\nabla^2\mathbf{u}_c \; in \; \Omega_c \; (11)$$

221   where the velocity field in the capillary domain, Ω_c, is given by $\mathbf{u}_c$. The boundary conditions are as

222   given in El-Bouri and Payne (2015): however, since we are not attempting to solve the equations

223   here, we will not consider the boundary conditions further as they are not directly relevant to the

224   derivation below. We define a small parameter $\varepsilon = d/D$ that relates the micro length scale, d, to

225   the macro length scale, D, as shown in Figure 1b (note that this definition of ε is only used in this

226   section).

227   We reduce the equations to non-dimensional form using the following scaling:

228
$$\mathbf{u}_c = U\mathbf{u}_c^* \; (12)$$

229
$$p = \frac{\mu DU}{d^2}p^* + p_0 \; (13)$$

230
$$\mathbf{X} = d\mathbf{X}^* \; (14)$$

231   based on a characteristic velocity U, capillary length scale d, voxel length scale D, and a characteristic

232   pressure that is based on viscous forces with an arbitrary offset. This scaling of pressure is based on

233   the fact that viscous forces dominate at the local scale and thus to bring the characteristic value of

234   pressure to the macro scale it is rescaled by ε^{-2}: this is due to the fact that the inter-capillary

235   spacing is of order ε and so there are of order ε^2 capillaries per unit area, meaning that pressure

236   scales with ε^{-2}. These characteristic values reduce Equation 11 to the following (where we drop the

237   star notation straight away for ease of notation):

238
$$\varepsilon Re_d(\mathbf{u}_c.\nabla)\mathbf{u}_c = -\nabla p_c + \varepsilon\mu\nabla^2\mathbf{u}_c \quad (15)$$

239 where Reynolds number on the micro scale is defined as:

240
$$Re_d = \frac{\rho U d}{\mu} \quad (16)$$

241 and the Reynolds number on the macro scale is therefore equal to $Re_D = Re_d/\varepsilon$. Since the problem

242 is more commonly formulated in terms of this parameter, Equation 15 thus becomes:

243
$$\varepsilon^2 Re_D(\mathbf{u}_c.\nabla)\mathbf{u}_c = -\nabla p_c + \varepsilon\mu\nabla^2\mathbf{u}_c \quad (17)$$

244 Since we consider the capillary bed relative to the larger vessels here, this gives micro and macro

245 length scales of approximately 100 μm and 1 cm respectively (noting that this analysis can be applied

246 to any separation of scales where the parameter ε is small). In this case, this parameter is equal to

247 approximately 0.01. For typical values of blood viscosity and density (3 mPa.s and 1040 kg/m^3

248 respectively), the macro Reynolds number is of order 1, where we assume a capillary velocity of

249 order 1 mm/s, see for example Unekawa et al. (2010). There is thus no need to re-scale Equation 17.

250 We now use a classical separation of scales approach. Since $\varepsilon \ll 1$, the local and macro length scales

251 are well separated and can be defined as $\mathbf{X}$ and $\mathbf{x} = \varepsilon\mathbf{X}$. Hence, using the standard approach, see for

252 example Holmes (2013), for separation of scales:

253
$$\nabla = \nabla_X + \varepsilon\nabla_x \quad (18)$$

254
$$\nabla^2 = \nabla_X^2 + 2\varepsilon\nabla_x.\nabla_X + \varepsilon^2\nabla_x^2 \quad (19)$$

255 and a multiple scales expansion:

256
$$\mathbf{u}_c = \mathbf{u}_c^0(\mathbf{x},\mathbf{X}) + \varepsilon\mathbf{u}_c^1(\mathbf{x},\mathbf{X}) + \varepsilon^2\mathbf{u}_c^2(\mathbf{x},\mathbf{X}) + \cdots \quad (20)$$

257
$$p = p^0(\mathbf{x},\mathbf{X}) + \varepsilon p^1(\mathbf{x},\mathbf{X}) + \varepsilon^2 p^2(\mathbf{x},\mathbf{X}) + \cdots \quad (21)$$

258   Substituting Equations 18-21 into the governing equation (Equation 17) orders of ε can now be

259   compared.

260   First in ε^0:

261
$$\nabla_X p^0 = 0 \ (22)$$

262   and then in ε^1:

263
$$\nabla_X p^1 + \nabla_x p^0 = \nabla_X^2 \mathbf{u}_c^0 \ (23)$$

264   Equations 22 and 23 can be solved along the lines proposed by Shipley and Chapman (2012) and as

265   performed in the cerebral microvasculature by El-Bouri and Payne (2015): these two equations are

266   sufficient to solve to leading order. The full derivation is given in Appendix A, with the end result

267   being a volume-averaged Darcy equation:

268
$$\langle \mathbf{u}_c^{(0)} \rangle_{\Omega_c} = -\mathbf{K}\nabla_x p_c^{(0)} \ (24)$$

269   where the permeability tensor, $\mathbf{K}$, is given in full in Appendix A. The advection term thus plays no

270   role in this context at leading order and can be considered only as a small correction term.

271   These two results thus combine to show that the advection term can be neglected in both individual

272   vessels (under the condition given above) and in the microvasculature when treated as a continuum.

273   This is a very important result, as it removes the only non-linear term in the Navier-Stokes equations.

274   Based on this result, we can utilise a wide range of results based on linear theory. It is worth noting

275   in passing that a number of authors have neglected the advection term by linearizing the governing

276   equations about a zero mean velocity, see for example Flores et al. (2016). Although the final result

277   obtained is the same, this linearization is, strictly speaking, unnecessary and can appear to limit the

278   validity of the solution. The results above offer a more rigorous and general proof that has a simple

279   condition: one that we will examine in more detail in the context of the cerebral circulation later.

2.2 Result 2: A first order differential model relating inlet and outlet flows to inlet and outlet

pressures in a vessel can be used when $\alpha < 1$ (α is Womersley number)

Having considered the flow as continuous in the second half of the result above, we now return to

consideration of a single vessel, as shown in Figure 1a. The aim here is to solve for the flow field such

that a relationship can be derived between the inlet and outlet flows and the inlet and outlet

pressures. In this way a simple relationship can be used for the flow in and out of each vessel in a

network such that a network of vessels can be connected together, using the results presented later.

In Result 1, we showed that the advection term can be neglected. As a result the governing

equations for flow in a single compliant vessel (the area-averaged Navier-Stokes equations coupled

with an elastic wall model) reduce to a linear form, enabling them to be transformed into the

frequency domain and written in the following form:

$$\hat{p}'' = \left(\frac{i\omega ZC}{L^2}\right)\hat{p} \ (25)$$

where:

$$Z = \mathcal{R}\frac{i\alpha^2}{8}\left[1 - \frac{2}{\alpha i^{3/2}}\frac{J_1(\alpha i^{3/2})}{J_0(\alpha i^{3/2})}\right]^{-1} \ (26)$$

and impedance, Z, resistance, $\mathcal{R}$, and compliance, C, are defined here for the whole vessel, of length

L . J_0 and J_1 denote Bessel functions of the first kind. We omit the dependence on frequency for

clarity, since the overhat denotes that the variable has been transformed into the frequency domain.

Womersley number is denoted by $\alpha = R\sqrt{\omega/\nu}$ and can be considered to be the ratio of oscillatory

inertial forces to shear forces. The derivation for these equations is based on the results of

Womersley (1955) and can be found in full in Flores et al. (2016). A schematic of the single vessel

model is shown in Figure 1a: we now consider this single vessel in this section without further

reference to the continuum model.

302   We can then use a perturbation series for pressure:

$$\hat{p} = \hat{p}_0 + \varepsilon\hat{p}_1 + \varepsilon^2\hat{p}_2 \dots (27)$$

304   in the small parameter, ε, defined in this section as:

$$\varepsilon = \alpha i^{3/2} \ (28)$$

306   We will examine the magnitude of this parameter later, but note that for the moment we are simply

307   assuming that it has magnitude less than one. Note that this is a different definition for ε from that

308   used in Section 2.1: we use this definition here as it is the standard notation for perturbation

309   methods and thus enables results obtained here to be easily compared with equivalent results

310   elsewhere.

311   Substituting Equation 28 into Equation 26 and Equations 26 and 27 into Equation 25 then yields:

$$[\varepsilon J_0(\varepsilon) - 2J_1(\varepsilon)](\hat{p}_0'' + \varepsilon\hat{p}_1'' + \varepsilon^2\hat{p}_2'' \dots) = \varepsilon^5 \left(\frac{\nu\mathcal{R}C}{8L^2R^2}\right) J_0(\varepsilon)(\hat{p}_0 + \varepsilon\hat{p}_1 + \varepsilon^2\hat{p}_2 \dots) \ (29)$$

313   We next convert the variables to non-dimensional form, such that pressure is computed relative to a

314   reference value (the value of this is irrelevant, since both sides of Equation 29 are linearly

315   proportional to pressure) and length relative to the length of the vessel, L. The prime thus becomes

316   relative to fractional length along the vessel. The problem is then defined in just two parameters, ε,

317   and:

$$\beta = \frac{\nu\mathcal{R}C}{8R^2} \ (30)$$

319   where resistance and compliance are equal to:

$$\mathcal{R} = \frac{8\mu L}{\pi R^4} \ (31)$$

$$C = L\frac{dA}{dp} \ (32)$$

322 The non-dimensional parameter β is of similar form to the (inverse square of) Womersley number,

323 but based on the time constant of the vessel (where $T = \mathcal{R}C$, as defined later) rather than the

324 oscillation frequency. The behaviour of each vessel is thus governed by the relative magnitudes of

325 these two non-dimensional groups.

326 To calculate the pressure series, we next use the series expansion of the Bessel functions,

327 Abramowitz and Stegun (1964):

328
$$J_0(x) = \sum_{i=0}^{\infty} \frac{(-1)^k}{2^{2k}(k!)^2} x^{2k} = 1 - \frac{x^2}{4} + \frac{x^4}{64} - \frac{x^6}{2304} + \cdots \quad (33)$$

329
$$J_1(x) = \sum_{i=0}^{\infty} \frac{(-1)^k}{2^{2k+1} k! \, (k+1)!} x^{2k+1} = \frac{x}{2} - \frac{x^3}{16} + \frac{x^5}{384} - \frac{x^7}{18432} + \cdots \quad (34)$$

330 Balancing terms in ascending powers of ε gives:

331
$$\hat{p}_0'' = 0 \quad (35)$$

332 which means that the pressure field to zeroth order is linear, set by the inlet and outlet boundary

333 conditions, as would be expected;

334
$$\hat{p}_1'' = 0 \quad (36)$$

335 which means that the first order pressure field is zero everywhere, since the inlet and outlet

336 boundary conditions at first and higher orders are zero;

337
$$\hat{p}_2'' = -8\beta\hat{p}_0 \quad (37)$$

338 which can be solved as described below;

339
$$\hat{p}_3'' = 0 \quad (38)$$

340 which means that the third order pressure field is also zero everywhere; and

341
$$\hat{p}_4'' = -8\beta \left[\hat{p}_2 - \frac{1}{6}\hat{p}_0 \right] (39)$$

342 We can now proceed to solve for the pressure field in the vessel up to this order. Equation 35 can be

343 solved using the inlet and outlet boundary conditions, defined here to be:

344
$$\hat{p}_0(x = 0) = \hat{p}_{in} (40)$$

345
$$\hat{p}_0(x = 1) = \hat{p}_{out} (41)$$

346 noting that these boundary conditions can of course be dynamically varying, since this is the solution

347 in the frequency domain, which can easily be inverted into the time domain. The zeroth order

348 pressure field is:

349
$$\hat{p}_0 = \hat{p}_{in}(1 - x) + \hat{p}_{out}x (42)$$

350 The resulting second order expression is calculated by substitution of Equation 42 into Equation 37

351 and solving given zero boundary conditions:

352
$$\hat{p}_2 = \hat{p}_{in}\frac{4\beta}{3}x(1 - x)(2 - x) + \hat{p}_{out}\frac{4\beta}{3}x(1 - x^2) (43)$$

353 and the fourth order expression similarly using Equations 42, 43 and 39:

354
$$\hat{p}_4 = -8\beta \left[\hat{p}_{in}x(1 - x)\left\{-\frac{\beta}{45}(3x^3 - 12x^2 + 8x - 8) + \frac{1}{36}(2 - x)\right\} \right.$$

355
$$\left. + \hat{p}_{out}x(1 - x)\left\{\frac{\beta}{45}(3x^3 + 3x^2 - 7x - 7) + \frac{1}{36}(1 + x)\right\} \right] (44)$$

356 The full solution is then:

357
$$\hat{p} = \hat{p}_0 + \varepsilon^2\hat{p}_2 + \varepsilon^4\hat{p}_4 \dots (45)$$

358 It should be noted that the expansion has been performed in terms of ε, but gives an expansion in

359 terms of even powers of ε, where ε is proportional to the square root of frequency: hence the

360 expansion is in integer powers of frequency.

361   Given the solution for the pressure field in the vessel, the flow field in the vessel can be calculated.

362   This is most easily done using a second perturbation series for flow of the form:

363
$$\hat{q} = \hat{q}_0 + \varepsilon\hat{q}_1 + \varepsilon^2\hat{q}_2 \dots (46)$$

364   where we substitute this into the expression for impedance:

365
$$\hat{q} = -\frac{1}{Z}\hat{p}' \ (47)$$

366   where the impedance is given by Equation 26 and the pressure by Equation 45, to obtain an

367   expression along the lines of Equation 29. We then calculate the flow field by balancing terms in

368   powers of ε, as done for the pressure field earlier, to give:

369
$$\hat{q}_0 = -\frac{1}{\mathcal{R}}\hat{p}_0' \ (48)$$

370
$$\hat{q}_2 = -\frac{1}{\mathcal{R}}\left[\hat{p}_2' + \frac{1}{6}\hat{p}_0'\right] \ (49)$$

371
$$\hat{q}_4 = -\frac{1}{\mathcal{R}}\left[\hat{p}_4' + \frac{1}{6}\hat{p}_2' + \frac{11}{384}\hat{p}_0'\right] \ (50)$$

372   where the differentials are again relative to non-dimensional length. Equations 42-44 can then be

373   substituted into these equations to derive an expression for the whole flow field. Most usefully,

374   however, the inlet and outlet flows can be calculated in terms of the inlet and outlet pressures. Since

375   these are linear, they are most easily written in matrix form:

376
$$\begin{pmatrix}\hat{q}_{in}\\\hat{q}_{out}\end{pmatrix} = \alpha_0\begin{pmatrix}\hat{p}_{in}\\\hat{p}_{out}\end{pmatrix} + \alpha_2\varepsilon^2\begin{pmatrix}\hat{p}_{in}\\\hat{p}_{out}\end{pmatrix} + \alpha_4\varepsilon^4\begin{pmatrix}\hat{p}_{in}\\\hat{p}_{out}\end{pmatrix} + \cdots \ (51)$$

377   where:

378
$$\alpha_0 = \frac{1}{\mathcal{R}}\begin{pmatrix}1 & -1\\1 & -1\end{pmatrix} \ (52)$$

379
$$\alpha_2 = \frac{1}{6\mathcal{R}}\begin{pmatrix}1 & -1\\1 & -1\end{pmatrix} + \frac{4}{3}\frac{\beta}{\mathcal{R}}\begin{pmatrix}-2 & -1\\1 & 2\end{pmatrix} \ (53)$$

380
$$\boldsymbol{\alpha}_4 = \frac{11}{384}\frac{1}{\mathcal{R}}\begin{pmatrix} 1 & -1 \\ 1 & -1 \end{pmatrix} + \frac{4}{9}\frac{\beta}{\mathcal{R}}\begin{pmatrix} 2 & 1 \\ -1 & -2 \end{pmatrix} + \frac{8}{45}\frac{\beta^2}{\mathcal{R}}\begin{pmatrix} -8 & -7 \\ 7 & 8 \end{pmatrix} \quad (54)$$

381   At zeroth order, i.e. steady state, the solution is exactly matched with the Poiseuille flow solution, i.e.

382   the inlet and outlet flows are equal to the driving pressure divided by the vessel resistance. The

383   Poiseuille solution is thus the leading order term in the dynamic solution. The second order

384   component of the solution (linearly proportional to frequency) then provides a dynamic 'correction'

385   that is dependent upon the non-dimensional group defined by Equation 30. This term is in turn

386   dependent upon both the vessel resistance and the compliance and hence dependent on both the

387   fluid and vessel properties. Note that the inlet and outlet can be swapped round and the formulation

388   will remain the same, as would be expected given the original equations. The fourth order

389   component is proportional to the square of frequency and can be neglected to a high degree of

390   accuracy (it is included here primarily for use in the following section).

391   As well as the frequency domain representation, it is useful to consider the results back in the time

392   domain. Considering Equation 51 and truncating the solution after terms up to ε^2 gives:

393
$$\begin{pmatrix} q_{in} \\ q_{out} \end{pmatrix} = \boldsymbol{\alpha}_0 \begin{pmatrix} p_{in} \\ p_{out} \end{pmatrix} - \frac{R^2}{\nu}\boldsymbol{\alpha}_2 \frac{d}{dt}\begin{pmatrix} p_{in} \\ p_{out} \end{pmatrix} \quad (55)$$

394   These (first-order differential) equations can then be used to relate the flows and pressures in each

395   vessel in a network, based on the two parameters β and $\mathcal{R}$, calculated for each vessel, by

396   substituting in the expressions for $\boldsymbol{\alpha}_0$ and $\boldsymbol{\alpha}_2$ given in Equations 52 and 53 respectively. For example,

397   in a single vessel, the inlet and outlet flows can be calculated directly from the inlet and outlet

398   pressures using Equation 55 and specific values of the two parameters. For a single vessel, the model

399   can be represented using two 2x2 matrices, relating the flows to the pressures; with the addition of

400   each vessel to a network, an additional unknown variable will be added, increasing the size of the

401   matrices by 1 in each dimension. This can then be done up to a network of arbitrary size, although it

402   is likely that alternative mathematical formulations would be used in very large networks due to the

403   computational cost.

404   For most networks this will be a sufficient representation, without the need for further terms: the

405   first term on the left hand side of Equation 55 is the 'traditional' term that relates steady flow to a

406   steady pressure difference along the vessel, with the second term adding in the dynamic effects that

407   occur due to the oscillation of the fluid and the interaction between the unsteady fluid motion and

408   an elastic wall. Note that the dynamic term thus exists even in a rigid vessel. We will consider in

409   more detail how these equations can be linked together later, once we have considered the

410   equations for volume and for connecting vessels in the next two sections, and then give an example

411   of the solution obtained using this approach.

2.3 Result 3: Blood volume can be modelled as quasi-steady-state when $\omega T \ll 180$ (ω is driving

frequency, *T* is vessel time constant)

414   In the previous result, we derived a relationship between the inlet and outlet flows and the driving

415   pressures in a single vessel, Figure 1a. This enables us directly to consider changes in the volume of

416   the vessel, *V*, through the difference between inlet and outlet flows:

$$\frac{dV}{dt} = q_{in} - q_{out} \quad (56)$$

418   In the frequency domain, using Equation 51 and Equation 56 gives:

$$i\omega\hat{V} = -4\frac{\beta}{\mathcal{R}}\varepsilon^2 (1 \quad 1)\begin{pmatrix}\hat{p}_{in}\\\hat{p}_{out}\end{pmatrix} + \varepsilon^4\frac{4}{9}\frac{\beta}{\mathcal{R}}\left(1 - \frac{2}{5}\beta\right)(1 \quad -1)\begin{pmatrix}\hat{p}_{in}\\\hat{p}_{out}\end{pmatrix} + \cdots \quad (57)$$

420   Substituting in Equation 28 and dividing by $i\omega$ (i.e. integrating) then gives:

$$\hat{V} = \frac{C}{2}(\hat{p}_{in} + \hat{p}_{out}) + i\omega\frac{R^2}{18\nu}\left(1 - \frac{2}{5}\beta\right)C(\hat{p}_{in} - \hat{p}_{out}) + \cdots \quad (58)$$

422   Hence to first order, the volume is equal to the product of compliance with average pressure, as

423   expected. The second term in Equation 58 is the dynamic component of volume changes: this is

424   particularly important in the context of localised changes in flow in response to activation. This

425   second term can be considered to be a 'dynamic' compliance term. If we assume that β is large

426   (strictly much larger than 5/2), then Equation 58 approximates to:

427
$$\hat{V} = \frac{C}{2}(\hat{p}_{in} + \hat{p}_{out}) - i\omega\frac{\beta R^2}{45\nu}C(\hat{p}_{in} - \hat{p}_{out}) + \cdots \quad (59)$$

428   We then formally define the product of resistance and compliance to be the time constant of the

429   vessel:

430
$$T = \mathcal{R}C \quad (60)$$

431   and hence Equation 59 simplifies to (eliminating β using Equation 30):

432
$$\hat{V} = \frac{C}{2}\left[(\hat{p}_{in} + \hat{p}_{out}) - \frac{i\omega T}{180}(\hat{p}_{in} - \hat{p}_{out}) + \cdots\right] (61)$$

433   Hence, the dynamic component can be neglected when $\omega T \ll 180$. Note that in the case where β is

434   not much larger than 5/2, then the dynamic component in Equation 58 will depend primarily on the

435   square of Womersley number, which then should be much less than 18 for the dynamic component

436   to be negligible: since we have already discussed this in Section 2.3, we will not consider this case

437   further. For completeness, as in the previous section, we convert Equation 61 back to the time

438   domain:

439
$$V = \frac{C}{2}\left[(p_{in} + p_{out}) - \frac{T}{180}\frac{d}{dt}(p_{in} - p_{out}) + \cdots\right] (62)$$

440   However, under the condition above ($\omega T \ll 180$), the volume then essentially follows a quasi-

441   steady state dependence on the average pressure in the vessel as follows:

442
$$V = \frac{C}{2}(p_{in} + p_{out}) \quad (63)$$

443   Note of course that we have not considered the viscoelastic nature of the vessel wall, which would

444   of course influence the result; however, the oscillation of the fluid makes only a negligible

445   contribution to the effective compliance of the vessel under this condition.

2.4 Result 4: Matching of static pressure at nodes can be used when $\varepsilon Re_D \ll 100$ (ε is ratio of vessel radius to length, Re_D is Reynolds number based on vessel diameter)

In the previous two sections we have derived relationships for inlet and outlet flows and volume in a single vessel as a function of the inlet and outlet pressures. The final stage in modelling the cerebral vasculature is to connect the vessels together. The main consideration here is the choice of boundary conditions relating flows and pressures at the nodes that connect individual vessels. Once these have been determined, all of the flows and volumes can be determined.

The first boundary condition that is universally applied is conservation of flow at nodes, i.e. the flow entering a node and the flow exiting a node must balance at all times. However, there is less agreement over the second boundary condition, related to pressure; two approaches have been used, essentially assuming that either static pressure remains the same as flow passes from one vessel into the next (as the flow velocity changes, this means that energy is not conserved), or that total pressure (and hence energy) is conserved, as discussed in the Introduction. The former approach however has the advantage that it is a linear condition and thus results in less computationally expensive numerical solutions. We thus examine in this section whether or not there is a significant difference between the two approaches.

We consider a bifurcating node, as shown in Figure 1c, where a parent vessel supplies two child vessels, where the inlet and outlet to the parent vessel are termed nodes 1 and 2a respectively, and the inlet to both child vessels is termed node 2b, i.e. points 2a and 2b are taken to be immediately before and after the node. If we assume identical conditions in both child vessels, the velocities are in the ratio:

$$\frac{u_C}{u_P} = \frac{1}{2}\left(\frac{R_P}{R_C}\right)^2 \quad (64)$$

468   relative to that in the parent vessel, from conservation of flow, where the subscripts P and C refer to

469   conditions in the parent and child vessels respectively. If we next assume Murray's law, Murray

470   (1926), with exponent n, we can also calculate the ratio of the vessel radii:

471
$$(R_P)^n = (R_C)^n + (R_C)^n = 2(R_C)^n \ (65)$$

472   since we are assuming identical child vessels. Hence:

473
$$\frac{u_C}{u_P} = \frac{1}{2}\left(2^{1/n}\right)^2 = 2^{\left(-1+\frac{2}{n}\right)} \ (66)$$

474   Matching total pressure at the node gives:

475
$$p_{2a} + \frac{1}{2}\rho u_P^2 = p_{2b} + \frac{1}{2}\rho u_C^2 \ (67)$$

476   We can thus calculate the change in pressure across the node, i.e. from the outlet of the parent

477   vessel to the inlet of the child vessel, as a fraction of the inlet velocity head:

478
$$C_p = \frac{p_{2b} - p_{2a}}{\frac{1}{2}\rho u_P^2} = 1 - 2^{\frac{2(2-n)}{n}} \ (68)$$

479   This is equal to 0 for n = 2, 0.18 for n = 7/3 and 0.37 for n = 3: these values being selected based on a

480   number of studies that have examined the value of this exponent in a number of scenarios, see for

481   example Mut et al. (2014). The largest value of this pressure coefficient is thus 0.37, which will tend

482   to occur at the smallest length scales as this is where n is closest to 3. Note that it is of course also

483   equal to 0 for the case of conservation of total pressure (the case where n = 2 is thus the only one

484   where both are matched). Now compare this to the pressure loss due to friction in the parent vessel:

485
$$C_p = \frac{p_1 - p_{2a}}{\frac{1}{2}\rho u_P^2} = \frac{32}{\varepsilon Re_D} \ (69)$$

486   where Reynolds number is here based on the parent vessel diameter, similar to Equation 4, and:

$$\varepsilon = \frac{R_P}{L_P} \quad (70)$$

487

488 is the radius to length ratio of the parent vessel (note that we again use ε in this section with a

489 different definition from earlier). This calculation for head loss is based on the assumption of laminar

490 flow (a reasonable approximation in this context since Reynolds number is low), as outlined in

491 standard fluid mechanics texts, see for example Caro et al. (2012).

492 Since the largest head loss coefficient at a node (Equation 68) is equal to 0.37, as shown above, this

493 is only comparable in magnitude to the head loss coefficient for an individual vessel (Equation 69)

494 when the product εRe_D is approximately 100. Hence, if this product is less than 100, the difference

495 between assuming matched static pressure and matched total pressure is small, since the head loss

496 across the node is small in comparison with the head loss along the upstream vessel. Since the

497 matching of static pressure results in linear equations, this can be used under this condition to

498 simplify the solution procedure without significant loss of accuracy. The question of whether static

499 or total pressure should be matched in the vessels where this condition does not hold is a difficult

500 one and one that needs further investigation but which is outside the scope of this paper.

501 **2.5 Result 5: Flow in a network can be solved using a series of matrices**

502 Based on Result 4, we can assume matched static pressure at nodes without any significant loss of

503 accuracy if $\varepsilon Re_D < 100$. The resulting equations for a network, for example that shown in Figure 1d,

504 can then be expressed in matrix form:

$$\boldsymbol{\alpha}_{int}\mathbf{p}_{int} = \boldsymbol{\alpha}_{ext}\mathbf{p}_{ext} \quad (71)$$

505

506 in terms of the (unknown) pressures at the internal nodes and the (known) pressures at the external

507 nodes. Equation 71 holds separately for each order of the solution. Once the matrices have been

508 formulated, Equation 71 can be solved for the unknown internal node pressures separately for each

509 order and the flows calculated through each vessel using the formulation above. Note that this can

510   be done in either the time domain or the frequency domain; in the latter case, it should be noted

511   that our approach, through exploitation of small values of Womersley number, is considerably

512   simpler than the method of Flores et al. (2016). The approach can of course be applied to networks

513   of arbitrary complexity as long as the assumptions are valid in every vessel, although for very large

514   networks it would be more likely that alternative methods (such as homogenisation techniques)

515   would be applied, see for example the approach proposed by El-Bouri and Payne (2015).

516   **3 Numerical simulations**

517   Having completed this analysis, we now consider the results in the context of previous models. In

518   particular we directly consider those models that model dynamic changes in the flow field. These

519   models, Boas et al. (2008), Reichold et al. (2009), Gagnon et al. (2015) and Payne and Lucas (2017),

520   are actually very similar in their approach, using a non-linear compliance model coupled with the

521   Poiseuille equation that uses an empirical model for viscosity based on vessel diameter and

522   haematocrit (which is taken to vary with vessel diameter). Although we have assumed a constant

523   compliance in our analysis here, we have shown that the assumption of quasi steady state (inherent

524   in all of the models listed above) is a valid one over all of the length scales that occur within the

525   cerebral vasculature.

526   However, we have shown in our analysis how to model the dynamic relationship between flow and

527   pressure in individual vessels and this has not been considered by the models listed above, where

528   only the leading order (Poiseuille) term is considered. Although the result given in Equation 55 is

529   more complicated, the dynamic term is not negligible in time-varying flow fields. We will illustrate

530   the effect that this can have in the simulations that we present below.

531   We consider the very simple bifurcating network shown in Figure 2 below, where we take the vessel

532   properties from the model proposed by Payne and Lucas (2017), as given in Table 2. We use this

533   network model as it is very similar to that proposed by Boas et al. (2008), where different modelling

534   assumptions were applied, as we will discuss below. It thus provides a simple means of comparison

535   of the dynamic behaviour of the model.
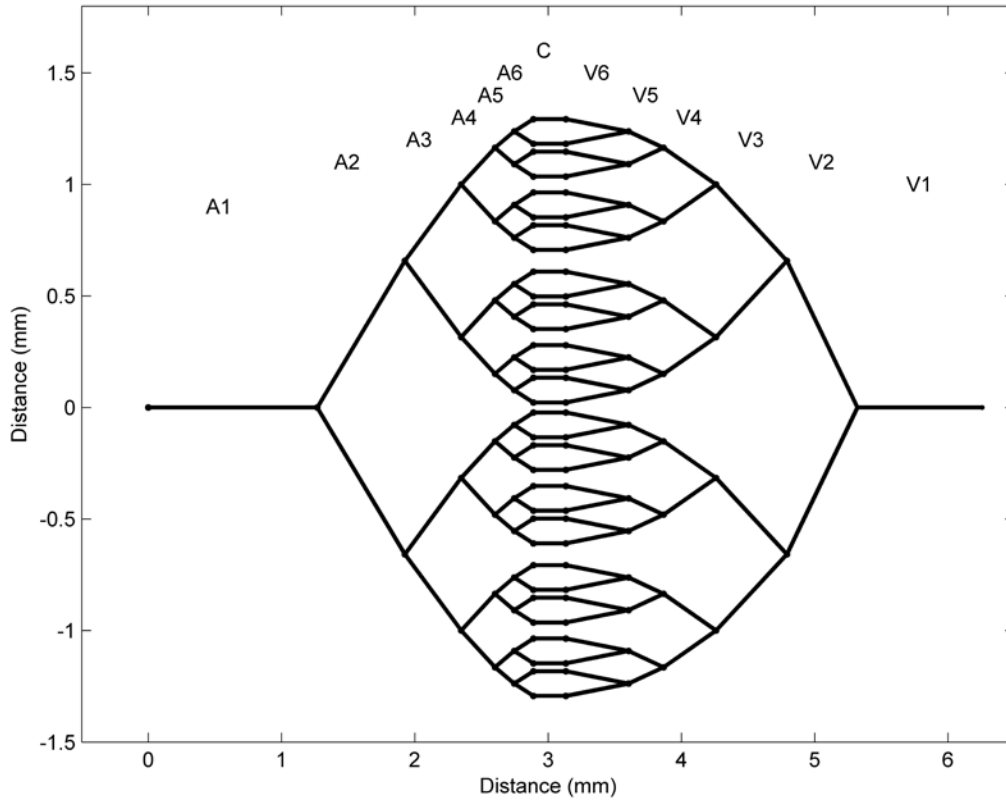
536

537   **Figure 2** Bifurcating network used in model simulations

Branch	Number of vessels	Diameter	Length	Wall thickness	Velocity	Viscosity	Pressure drop	Saturation
		μm	μm	μm	mm/s	mPa.s	mmHg	%
A1	1	23.97	1267.6	4.84	8.2	1.59	6.93	94
A2	2	19.17	930.3	4.25	6.41	1.50	5.87	93
A3	4	15.28	543.6	3.81	5.05	1.42	4.02	92
A4	8	12.08	302.3	3.49	4.03	1.34	2.70	89
A5	16	9.46	161.2	3.27	3.29	1.28	1.82	84

A6	32	7.32	154.7	3.14	2.75	1.23	2.35	76.5
C	64	8	243.9	0.309	2.30	1.24	2.62	66.5
V6	32	11.51	473.9	1.15	1.11	1.33	1.27	61
V5	16	14.53	272.3	1.45	1.40	1.40	0.61	59.75
V4	8	17.79	426.6	1.78	1.86	1.48	0.89	58.75
V3	4	21.45	632.5	2.15	2.56	1.55	1.31	58.25
V2	2	25.70	844.2	2.57	3.57	1.62	1.78	57.75
V1	1	30.77	936.3	3.08	4.97	1.70	2.01	57.25

Table 2 Vascular parameters used in network model

For comparison, we plot the results obtained for the same network but using the flow and volume model proposed by Boas et al. (2008) and used by other authors; the equations in this and in our model are set out for comparison and for convenience of reference in Table 3. This approach assumes that there is an instantaneous equilibrium between flow and pressure:

$$q_{ij} = \frac{1}{\mathcal{R}_{ij}} \left(p_i - p_j \right) \quad (72)$$

between nodes i and j, i.e. as Equation 55, but neglecting all dynamic terms. It then assumes that the volume of each vessel, V_i, follows changes in pressure through a non-linear relationship of the form:

$$p_i - p_{ic} = kV_i^{\beta} \quad (73)$$

where k is a constant, set by baseline conditions, and β is a compliance parameter that is set to 2 by Boas et al. (2008). The loop of equations is closed by conservation of volume:

$$\frac{dV_i}{dt} = q_{i,in} - q_{i,out} \quad (74)$$

These equations can easily be solved dynamically for the same dynamic inlet pressure and network parameters given above.

	New approach	**Previous approach**
Pressure-flow relationship	$\begin{pmatrix} q_{in} \\ q_{out} \end{pmatrix} = \boldsymbol{\alpha}_0 \begin{pmatrix} p_{in} \\ p_{out} \end{pmatrix} - \frac{R^2}{v} \boldsymbol{\alpha}_2 \frac{d}{dt} \begin{pmatrix} p_{in} \\ p_{out} \end{pmatrix}$ (Equation 55)	$q_{ij} = \frac{1}{\mathcal{R}_{ij}} (p_i - p_j)$ (Equation 72)
Pressure-volume relationship	$V = \frac{C}{2} (p_{in} + p_{out})$ (Equation 63)	$p_i - p_{ic} = kV_i^{\beta}$ (Equation 73)
Flow-volume relationship	$\frac{dV}{dt} = q_{in} - q_{out}$ (Equation 56)	$\frac{dV_i}{dt} = q_{i,in} - q_{i,out}$ (Equation 74)
Nodal relationship	Conservation of flow Matching of static pressure	Conservation of flow Matching of static pressure

Table 3 Summary of model equations in both approaches; for terminology, see original equations

We now illustrate our approach by considering the response to changes in inlet pressure. For simplicity, we assume a reduction in inlet pressure from 60 mmHg to 48 mmHg (a drop of 20 %). In order to give a smoothly varying inlet pressure, we assume a function of the form:

$$p_{in} = P_a \left[1 + \left(\frac{k-1}{2} \right) \left(1 + \tanh \left(\frac{t-1}{0.1} \right) \right) \right] \quad (75)$$

with k denoting the fractional value of baseline pressure to which the function tends, set here to 0.8 (i.e. a 20 % drop in driving pressure). This drop occurs at a time of 1 second (allowing the model to settle before the change occurs) with a rapid rate of change. The resulting changes in nodal pressure and vessel volume across all 13 generations are then calculated using both sets of model equations set out in Table 4.

We first examine the changes in blood pressure within the network. Since our new approach is based on nodal pressures and the previous approach on pressures in the middle of the vessel, we interpolate the nodal pressures to plot the pressures half way along the vessels. We plot the pressures in the third generation of the arteriolar bed, in the capillary bed, and in the fourth

566   generation of the venous bed for both models, as shown in Figure 3. We assume a value of 10 mmHg

567   for intracranial pressure and an exponent of 1 in Equation 73; we then calculate the value of k from

568   baseline conditions.

569   It is clear from Figure 3 that the changes in pressure propagate downstream from inlet to outlet,

570   with the largest and fastest changes occurring at the vessels closest to the inlet. Whilst the response

571   times to changes in inlet blood pressure in these vessels is of order only a couple of seconds, as

572   shown in Figure 3, we note that the response is not instantaneous, and care thus needs to be taken

573   in calculating the flow response to changes in inlet pressure since there is a delay in the propagation

574   of pressure changes through the network. Without considering the delay, there would be an

575   instantaneous response in all vessels.

576   The previous model exhibits a much faster response throughout the vasculature; this is caused by

577   neglecting the second term in Equation 55. As a result, the speed of response is substantially

578   different; our model shows how the dynamic term in Equation 55 does play an important role in

579   setting the speed of response, even at this small length scale. Estimating the time constant of the

580   response yields values of 0.17, 0.76 and 1.15 seconds in our new model for the mid-arteriolar,

581   capillary and mid-venous vessels respectively, compared to 0.14, 0.34 and 0.47 seconds for the

582   previous model, showing how although the earlier vessels respond at a similar speed, the later

583   vessels respond much more slowly.

584
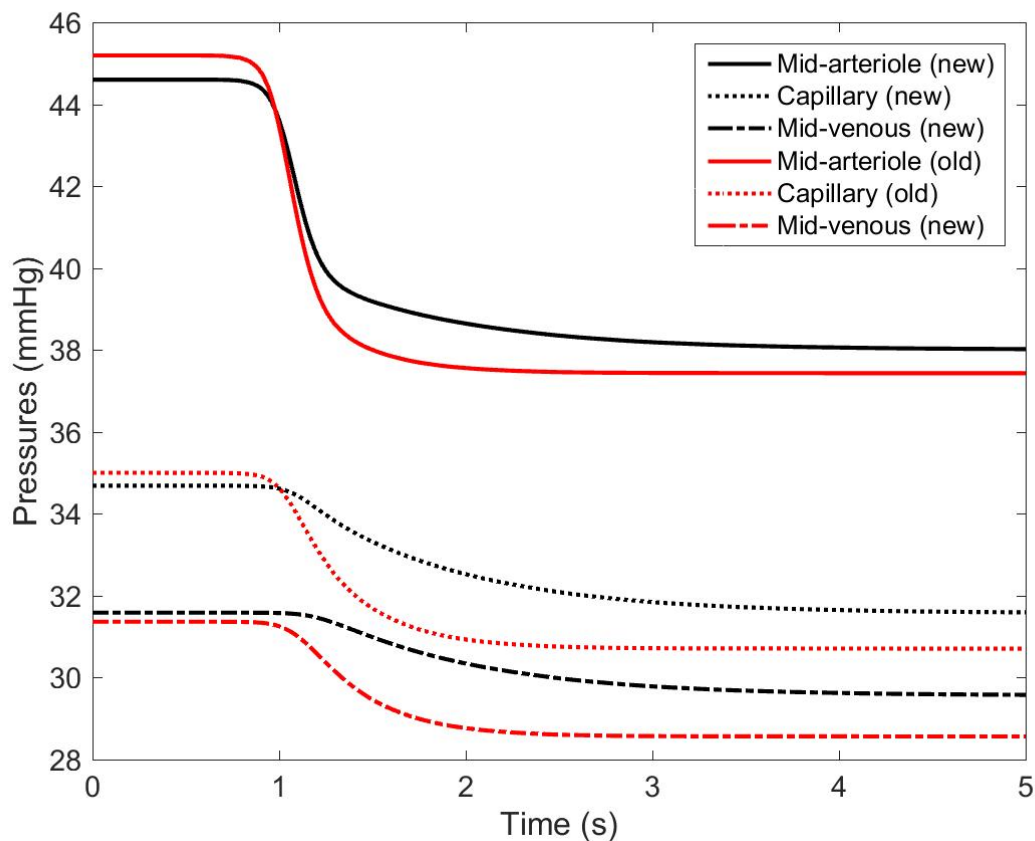
Figure 3 Dynamic changes in blood pressures in bifurcating network in response to 20 % decrease in

inlet blood pressure (for definitions of locations, see main text)

587   The results for volume, Figure 4, follow those for pressure, as would be expected from the analysis

588   above and the justification of quasi steady state behaviour in response to changes in pressure. The

589   later generations of the network thus respond much more slowly in response to changes in inlet

590   blood pressure than would be assumed from the previous modelling approach. This difference is

591   caused by the fact that previous approaches assumed a dynamically varying volume in response to

592   instantaneous changes in pressure: our analysis shows rather that pressure responds dynamically to

593   changes in inlet conditions with volume following these pressure changes quasi-statically (and hence

594   with the same delay as the pressure changes).

595
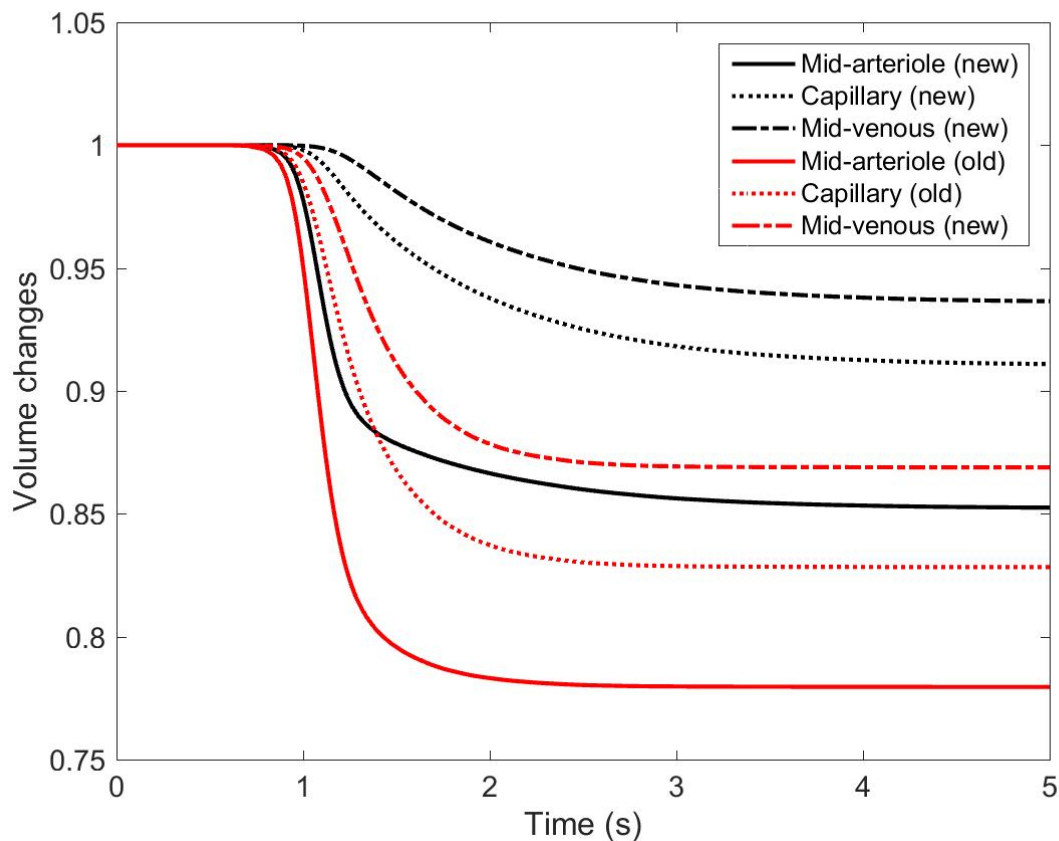
Figure 4 Dynamic changes in blood volumes in bifurcating network in bifurcating network in

response to 20 % decrease in inlet blood pressure (for definitions of locations, see main text)

598   This is an important distinction and the fact that the changes in pressure and volume have now been

599   shown to be slower than previously thought will significantly alter the dynamic behaviour of

600   pressure and volume changes in models of the cerebral microvasculature. Note that the differences

601   in absolute values of volumes between the two models, shown in Figure 4, are due to the slightly

602   different models that are used for compliance in the two approaches; however this does not affect

603   the main finding of this study. Experimental validation, through simultaneous measurements of

604   blood flow and blood volume will be extremely valuable in validating the approach set out here and

605   quantifying the importance of the dynamic term in Equation 55.

606   **4 Discussion**

607   In the previous section we have shown that the non-linear advection term can be neglected, when

608   considering both single vessels and the flow field as a continuum; derived a relationship between

609   inlet and outlet flows in single vessels and inlet and outlet pressures; derived the condition for a

610   quasi-steady-state approximation for blood volume; and then shown how single vessels can be

611   linked together and the flow field in a network solved as a matrix problem. For each of these

612   derivations there is a limit on the validity of the approximation: we thus consider these now in the

613   particular context of the cerebral vasculature. We will then also consider the limitations of the

614   approach that we have adopted. We should note that since we are basing many of the assumptions

615   on order of magnitude arguments, the precise values are often less important than the relative

616   magnitudes of different parameters.

617   We will assume throughout this section that blood has a density of 1040 kg/m^3 and a kinematic

618   viscosity of approximately 3 μPa.s (we will consider the value of viscosity in more detail below) and

619   that the oscillation frequency is approximately 1 Hz (based on a typical heart rate of around 60 beats

620   per minute), see for example Caro et al. (2012). We can therefore quantify the magnitude of the

621   Womersley number immediately. This has magnitude less than one in vessels smaller than

622   approximately 1.4 mm in diameter. The first order model presented in Result 2 is thus only valid for

623   vessels of such diameter. Since the lower limit for imaging individual vessels is down to those with

624   diameters of approximately 0.8-0.9 mm, see for example Mut et al. (2014), this approach does thus

625   cover all of the generations of 'unseen' vessels and can therefore be applied to these vessels, i.e.

626   those of diameter less than approximately 1.4 mm.

627   We next consider the product ωT. As a first approximation, we assume the same elastic isotropic

628   model of the vessel wall as in Section 2.1; this then yields, see for example Chappell and Payne

629   (2016):

$$\omega T = 12 \left(\frac{\mu\omega}{E}\right)\left(\frac{L^2}{Rh}\right) \quad (76)$$

630

631   where the right hand side comprises non-dimensional groups, as shown in brackets, the latter based

632   on the geometry of the vessel and the former based on a mixture of properties. If we assume a value

633   of wall Young's modulus of 10^4 Pa, Caro et al. (2012), then this former term is approximately equal to

634   2 x 10^{-6}. The condition for the quasi-steady-state volume relationship then becomes

635   approximately Rh/L^2 > 1.2×10^{-7}, which is satisfied by every vessel in the cerebral vasculature, since

636   the radius to length ratio is rarely less than 0.01 and the wall thickness to radius ratio is normally in

637   the range 0.1 to 0.5, see for example Payne (2007), Lucas (2012), Caro et al. (2012) and Payne (2017).

638   It is worth noting that this is in good agreement with recent studies into the neurovascular coupling

639   response, which have indicated a relatively small volume component to the short term response,

640   Hillman et al. (2007), Vazquez et al. (2010) and Drew et al. (2011). It also points away from the use of

641   the delayed compliance model, Kong et al. (2004) and Zheng and Mayhew (2009), since the time

642   constant has been shown here to be negligible in all vessels in the cerebral vasculature.

643   We next consider the ratio $\frac{E}{\rho U^2}\frac{h}{R}$, which needs to be much greater than 3/2 for advection to be

644   neglected. Since the ratio of wall thickness to radius, $\frac{h}{R}$, is typically in the range 0.1 to 0.5 (see above)

645   in any vessel, a lower bound for this can be taken to be 0.1: the ratio $\frac{E}{\rho U^2}$ needs to be much greater

646   than approximately 15. The flow velocity thus needs to be much less than $\sqrt{E/15\rho}$, which, for the

647   values of wall Young's modulus and blood density quoted above, is equivalent to being much less

648   than approximately 0.8 m/s. This is well above any flow velocity found in the cerebral vasculature

649   under normal conditions, Lucas (2012) and Payne (2017), and thus advection terms can be neglected

650   throughout the cerebral vasculature, although it should be noted that under certain conditions, for

651   example severe stenosis, flow velocities can rise substantially and that care would have to be taken

652   under such circumstances to re-evaluate this approximation.

653   Finally, we consider the product εRe_D, which should be below 100 for the difference between

654   matching of static and total pressures to be negligible. In the largest blood vessels in the brain, the

655 flow velocity is of order 0.5 m/s with diameters of order 5 mm, see for example Lucas (2012). Such

656 values give a Reynolds number based on diameter of approximately 1000. Since the typical radius to

657 length ratio values found in these large vessels are of order 0.1, Mut et al. (2014), the product εRe_D

658 is thus of order 100 in the largest vessels in the brain. The difference between matched static and

659 matched total pressure can thus be significant in these largest vessels; however, in the vessels below

660 the imaging threshold of approximately 1 mm in diameter, Mut et al. (2014), this ratio will be below

661 this limit, making the matching of static pressure a justifiable assumption in such vessels. Care simply

662 needs to be taken when modelling the larger vessels, essentially those that can be imaged directly.

663 In these vessels, the product εRe_D can be calculated for each vessel and the assumption of matched

664 static pressure examined in each individual vessel.

665 We have thus explored how the four relationships derived earlier relate to individual blood vessels in

666 the cerebral vasculature. It has been shown that advection can always be neglected in the equation

667 governing blood flow and that blood volume can be assumed to be in quasi-steady state at all times;

668 however, the first order approach for pressure and flow (arising from the perturbation series

669 analysis) and the matching of static pressure should only be applied in vessels below approximately

670 1 mm in diameter (using this as an approximate threshold for the distinction). Since this

671 approximately corresponds to the imaging threshold, it is then possible to apply all four

672 simplifications to models at this length scale. This does make the application of such models

673 significantly easier. For simplicity we summarise these results in Table 4 below.

	Vessels of diameter < 1 mm	Vessel of diameter > 1 mm
Neglect advection	Yes	Yes
First order model	Yes	No
Blood volume quasi steady state	Yes	Yes
Match static pressure	Yes	Possibly

674 **Table 4** List of assumptions in vessels of different diameter

675 Note that whilst we have considered every vessel in each generation to respond in exactly the same

676 manner, due to the symmetry of the change that we have imposed (and for simplicity of

677 presentation), it would easily be possible to consider the response to localised changes in individual

678 vessels, as has been examined by other authors; although it should be noted that this model is at

679 present a purely passive one and that a model of the active response should be coupled with this

680 model in future to provide good agreement with experimental data, for example examining the

681 response to activation, as discussed in the Introduction.

682 It would be possible to characterise the overall behaviour of the network in terms of lumped values

683 of resistance and compliance, reducing the network to simpler form: characterising the response of

684 the network to changes in terms of time constants would be a valuable exercise, since this enables

685 the behaviour of the network to be considered as a whole, along the lines of the 6 second time

686 constant for oxygen transport in the same network found by Payne and Lucas (2017). This would

687 help to construct more detailed models of the larger vasculature, of which this network is only one

688 very small part. However, the approach set out in Table 3 under the restrictions set out in Table 4

689 can be used across the cerebral vasculature and it is suggested that these modelling equations,

690 validated by the analysis presented earlier, be used in this context in place of the other approaches

691 that have been used.

692 It is worth noting that alongside the model framework presented here that considers each vessel

693 individually, we also discussed earlier the use of a continuous approach to flow in the

694 microvasculature, based on the work of El-Bouri and Payne (2015) in providing a Darcy

695 approximation for the capillary flow field, as presented above, that has been coupled to a network

696 model in El-Bouri and Payne (2018), as shown in Figure 1d. This approach offers a complementary

697 method to the 'discrete' flow field presented here, since the two approaches can be coupled

698 together, dependent upon the length scale being considered and the size of the network that is

699   being studied, potentially reducing the computation time very significantly by exploiting the wide

700   range of length scales.

701   We do note that there are a number of limitations to the analysis above. We have assumed

702   axisymmetric vessels and flow fields, which is a reasonable assumption to these flows, although care

703   should be taken when considering vessels with any significant tortuosity. A more significant

704   assumption, however, is that we have assumed the fluid to be Newtonian, which does limit the

705   analysis. However, since the non-Newtonian effects will be greatest in the smaller vessels, which we

706   have found to be furthest away from the limits derived here, it thus seems reasonable to assume

707   that the non-Newtonian effects will have little impact on the results found here, although a more

708   rigorous analysis would be required to justify this more completely.

709   We have also neglected variations in haematocrit, which can have a significant impact on the flow

710   field throughout microvascular networks, Gould and Linninger (2015). The choice of model for

711   haematocrit distribution can also strongly influence the local flow patterns, although further

712   examination of the effects of this on the overall network behaviour is still needed. It would be

713   extremely interesting to examine the effects of the variability in haematocrit distribution on the

714   results that we have presented here.

715   In addition to this, future work will also involve extending the analysis to the transport of oxygen and

716   glucose between blood and tissue, using the approach set out in Payne and Lucas (2017), since

717   solving these equations is key to understanding the relationship between flow and metabolism. The

718   coupled nature of the equations means that this is a more difficult problem to investigate, although

719   considerable progress has been made by many of the studies listed in the Introduction. However, by

720   doing so, it will be possible to develop more rigorous models of both flow and metabolism that will

721   hopefully help to provide more insight into their behaviour in both normal and abnormal

722   physiological conditions.

723   This will also help to link to models of the BOLD response, providing a sounder theoretical

724   justification for the haemodynamic components of such models, in particular the lumped parameter

725   components, which often have to be assumed on a somewhat ad hoc basis, see for example Aquino

726   et al. (2014). Such multi-scale modelling approaches have a great deal to offer in terms of

727   understanding the relationship between the underlying physiology and experimental measurements

728   and provide a rich avenue for exploration in the future. They also offer the possibility of

729   experimental validation through the characterisation of models over different length scales, enabling

730   the assumptions used in the model proposed here to be more directly tested, using potentially a

731   very wide range of measurement modalities, including but not restricted to BOLD, MRI and PET.

732

733 **Appendix A**

734 A fundamental assumption when using homogenization is that the large-scale structure, in
735 this case the capillary bed, is locally periodic. This allows the removal of secular terms in
736 multi-dimensional problems without the need to solve higher order equations explicitly. It is
737 of course possible to homogenize non-locally periodic structures, however finding the
738 solvability condition to eliminate the secular terms becomes very difficult. Periodicity is thus
739 regularly used in homogenization to simplify the removal of secular terms and is used here.

740 As $\varepsilon \ll 1$ the local and macro length scales are well-separated and can be defined as $\mathbf{X}$ and
741 $\mathbf{x} = \varepsilon\mathbf{X}$ respectively. Using the assumption of scale separation both $\mathbf{x}$ and $\mathbf{X}$ can be treated
742 as independent variables and so

743
$$\nabla = \nabla_X + \varepsilon\nabla_x, \qquad \nabla^2 = \nabla_X^2 + 2\varepsilon\nabla_x.\nabla_X + \varepsilon^2\nabla_x^2 \text{ (A.1)}$$

744 Using this to expand out Equation 17 gives:

745
$$\varepsilon^2 Re_D[(\mathbf{u}_c.\nabla_X)\mathbf{u}_c + \varepsilon(\mathbf{u}_c.\nabla_x)\mathbf{u}_c] = -\nabla_X p_c - \varepsilon\nabla_x p_c + \varepsilon\nabla_X^2\mathbf{u}_c \\ + 2\varepsilon^2\nabla_x.\nabla_X\mathbf{u}_c + \varepsilon^3\nabla_x^2\mathbf{u}_c \text{ in } \Omega_c \text{ (A.2)}$$

746 We also use non-dimensional forms of the continuity equation and the boundary conditions:

747
$$\nabla_X.\mathbf{u}_c + \varepsilon\nabla_x.\mathbf{u}_c = 0 \text{ in } \Omega_c \text{ (A.3)}$$

748
$$\mathbf{u}_c.\boldsymbol{n} = 0 \text{ on } \Gamma_c \text{ (A.4)}$$

749
$$\mathbf{u}_c.\boldsymbol{\tau} = 0 \text{ on } \Gamma_c \text{ (A.5)}$$

750 where Ω_c denotes the blood space and Γ_c denotes the boundary between blood and tissue.
751 We then apply the multiple scales expansion for velocity and pressure given in Equations 20
752 and 21. In order to maintain periodicity each component of $\mathbf{u}$ and p is assumed to be
753 periodic in $\mathbf{X}$. The expansions of Equations 20 and 21 are substituted into Equations A.2-A.5
754 and successive orders of ε equated to determine the leading order homogenized equations
755 for capillary flow and pressure:

$$\varepsilon^2 Re_D[((\mathbf{u}_c^{(0)} + \varepsilon\mathbf{u}_c^{(1)} + \cdots).\nabla_X)(\mathbf{u}_c^{(0)} + \varepsilon\mathbf{u}_c^{(1)} + \cdots) +$$
$$\varepsilon((\mathbf{u}_c^{(0)} + \varepsilon\mathbf{u}_c^{(1)} + \cdots).\nabla_x)(\mathbf{u}_c^{(0)} + \varepsilon\mathbf{u}_c^{(1)} + \cdots)] =$$

756

$$-\nabla_X (p_c^{(0)} + \varepsilon p_c^{(1)} + \cdots) - \varepsilon\nabla_x(p_c^{(0)} + \varepsilon p_c^{(1)} + \cdots) + \varepsilon\nabla_X^2(\mathbf{u}_c^{(0)} + \varepsilon\mathbf{u}_c^{(1)} + \cdots)$$
$$+ 2\varepsilon^2\nabla_x.\nabla_X\left(\mathbf{u}_c^{(0)} + \varepsilon\mathbf{u}_c^{(1)} + \cdots\right) + \varepsilon^3\nabla_x^2\left(\mathbf{u}_c^{(0)} + \varepsilon\mathbf{u}_c^{(1)} + \cdots\right) \text{ in } \Omega_c \text{ (A.6)}$$

757
$$\nabla_X.\left(\mathbf{u}_c^{(0)} + \varepsilon\mathbf{u}_c^{(1)} + \cdots\right) + \varepsilon\nabla_x.\left(\mathbf{u}_c^{(0)} + \varepsilon\mathbf{u}_c^{(1)} + \cdots\right) = 0 \text{ in } \Omega_c \text{ (A.7)}$$

758
$$\left(\mathbf{u}_c^{(0)} + \varepsilon\mathbf{u}_c^{(1)} + \cdots\right).\boldsymbol{\tau} = 0 \text{ (A.8)}$$

759
$$\left(\mathbf{u}_c^{(0)} + \varepsilon\mathbf{u}_c^{(1)} + \cdots\right).\boldsymbol{n} = 0 \text{ (A.9)}$$

760   Equating powers of $O(\varepsilon^0)$ in Equations A.6-A.9 gives:

761
$$\nabla_X \, p_c^{(0)} = 0 \text{ (A.10)}$$

762
$$\nabla_X.\mathbf{u}_c^{(0)} = 0 \text{ (A.11)}$$

763
$$\mathbf{u}_c^{(0)}.\boldsymbol{\tau} = 0 \text{ and } \mathbf{u}_c^{(0)}.\boldsymbol{n} = 0 \text{ on } \Gamma \text{ (A.12)}$$

764   and equating powers of $O(\varepsilon^1)$:

765
$$\nabla_X \, p_c^{(1)} + \nabla_x p_c^{(0)} = \nabla_X^2\mathbf{u}_c^{(0)} \text{ (A.13)}$$

766
$$\nabla_X.\mathbf{u}_c^{(1)} + \nabla_x.\mathbf{u}_c^{(0)} = 0 \text{ (A.14)}$$

767
$$\mathbf{u}_c^{(1)}.\boldsymbol{\tau} = 0 \text{ and } \mathbf{u}_c^{(1)}.\boldsymbol{n} = 0 \text{ on } \Gamma \text{ (A.15)}$$

768   From Equation A.10 it is evident that $p_c^{(0)}$ is constant at the local-scale, hence $p_c^{(0)} = p_c^{(0)}(\mathbf{x})$.

769   In order to determine the leading order problem it is necessary to solve for $\mathbf{u}_c^{(0)}$ and $p_c^{(1)}$.

770   From Equation A.13 it can be seen that $\mathbf{u}_c^{(0)}$ and $p_c^{(1)}$ are both linear functions of $\nabla_x p_c^{(0)}$ and

771   so solutions are proposed of the form:

772
$$\mathbf{u}_c^{(0)} = -w_c^j(\mathbf{X})\frac{dp_c^{(0)}}{dx^j} \text{ (A.16)}$$

773
$$p_c^{(1)} = -P_c^j(\mathbf{X})\frac{dp_c^{(0)}}{dx^j} + \bar{p}_c^{(1)} \text{ (A.17)}$$

774   Einstein notation has been used here for clarity where j can take the values 1, 2, or 3 and

775   refers to the Cartesian co-ordinate directions. The notation used is a simple substitution for

776   what would otherwise be a dot product of the two j components. $\boldsymbol{w}_c^j(\mathbf{X})$ and $P_c^j(\mathbf{X})$ account

777   for the local variations in $\mathbf{u}_c^{(0)}$ and $p_c^{(1)}$ and are known as the cell variables. It is from these

778   local variables that the homogenized macro-scale parameters of the blood flow in the

779   capillary network can be determined. These variables are determined by inserting them into

780   Equations A.10-A.12 to obtain the cell problem:

781
$$\nabla_{\mathbf{X}} \cdot \boldsymbol{w}_c^j(\mathbf{X}) = 0 \quad \text{in } \Omega_c \text{ (A. 18)}$$

782
$$\nabla_{\mathbf{X}} P_c^j(\mathbf{X}) = \nabla_{\mathbf{X}}^2 \boldsymbol{w}_c^j(\mathbf{X}) + \mathbf{e}_j \quad \text{in } \Omega_c \text{ (A. 19)}$$

783
$$\boldsymbol{w}_c^j(\mathbf{X}) \cdot \boldsymbol{\tau} = 0 \text{ and } \boldsymbol{w}_c^j(\mathbf{X}) \cdot \boldsymbol{n} = 0 \quad \text{on } \Gamma \text{ (A. 20)}$$

784   where $\mathbf{e}_j$ is the unit vector in the j-direction. This is the local periodic cell problem which

785   must be solved numerically in order, as shall be seen, to derive the parameters for the

786   macro-scale problem. Note that Equation A.19 is a forced Stokes flow problem. From this is

787   derived the Poiseuille equation (making assumptions on the radial and swirl components of

788   the velocity). Therefore, despite having left in the convective acceleration term in the

789   original equations, to leading order the cell problem is Stokes flow.

790   From Equations A.19-A.20 it can be seen that the cell problem is underdetermined and

791   hence the local pressure term P_c^j is only defined up to a constant value. A uniqueness

792   condition is thus imposed which states that the volume average of the local pressure is zero:

793
$$\langle P_c^j \rangle_c = \frac{1}{|\Omega|} \int_{\Omega_c} P_c^j \, dV = 0 \text{ (A. 21)}$$

794   Taking a volume average over $\mathbf{u}_c^{(0)}$, Equation A.16 results in:

795
$$\langle \mathbf{u}_c^{(0)} \rangle_{\Omega_c} = -\mathbf{K} \nabla_x p_c^{(0)} \text{ (A. 22)}$$

796   where

797
$$K_{ij} = \frac{1}{|\Omega|} \int_{\Omega_c} w_{ci}^j \, dV \text{ (A. 23)}$$

798   This is Darcy's Law with **K** defining the permeability tensor. Therefore, to leading order, the

799   homogenization of the incompressible, steady state Navier-Stokes equations gives Darcy's

800   Law. The permeability tensor **K** encapsulates the geometry of the problem and how the

801   geometry affects the flow for given pressure gradients. It is an averaged coefficient tensor,

802   calculated by solving the micro cell problem, and is the volume average of the velocities in

803   the cell problem.

804

805 **References**

806 Abramowitz M, Stegun I. Handbook of Mathematical Functions. United States Department of

807   Commerce, National Bureau of Standards. 1964.

808 Acheson DJ. Elementary Fluid Dynamics. Oxford University Press. 1990.

809 Alastruey J, Parker KH, Peiró J, Byrd SM, Sherwin SJ. Modelling the circle of Willis to assess the

810   effects of anatomical variations and occlusions on cerebral flows. J Biomech. 2007;40(8):1794-

811   805.

812 Aquino KM, Robinson PA, Drysdale PM. Spatiotemporal hemodynamic response functions derived

813   from physiology. J Theor Biol. 2014 Apr 21;347:118-36. doi: 10.1016/j.jtbi.2013.12.027. Epub

814   2014 Jan 4.

815 Aquino KM, Robinson PA, Schira MM, Breakspear M. Deconvolution of neural dynamics from fMRI

816   data using a spatiotemporal hemodynamic response function. Neuroimage. 2014 Jul 1;94:203-

817   215. doi: 10.1016/j.neuroimage.2014.03.001. Epub 2014 Mar 12.

818 Blinder P, Shih AY, Rafie C, Kleinfeld D. Topological basis for the robust distribution of blood to

819   rodent neocortex. Proc Natl Acad Sci USA. 2010;107:12670–12675.

820 Boas DA, Jones SR, Devor A, Huppert TJ, Dale AM. A vascular anatomical network model of the

821   spatio-temporal response to brain activation. Neuroimage. 2008 Apr 15;40(3):1116-29.

822 Buxton RB, Wong EC, Frank LR. Dynamics of blood flow and oxygenation changes during brain

823   activation: the balloon model. Magn Reson Med. 1998 Jun;39(6):855-64.

824 Canic S, Kim EH. Mathematical analysis of the quasilinear effects in a hyperbolic model of blood flow

825   through compliant axi-symmetric vessels. Math. Meth. Appl. Sci. 2003; 26: 1161–1186.

826   Caro CG, Pedley TJ, Schroter RC and Seed WA. The mechanics of the circulation, 2nd edition.

827   Cambridge University Press, 2012.

828   Cassot F, Lauwers F, Fouard C, Prohaska S, Lauwers-Cances V. A novel three-dimensional computer-

829   assisted method for a quantitative study of microvascular networks of the human cerebral cortex.

830   Microcirculation. 2006 Jan;13(1):1-18.

831   Chappell MA, Payne SJ. Physiology for Engineers. Springer. 2016.

832   Drew PJ, Shih AY, Kleinfeld D. Fluctuating and sensory-induced vasodynamics in rodent cortex extend

833   arteriole capacity. Proc Natl Acad Sci U S A. 2011 May 17;108(20):8473-8. doi:

834   10.1073/pnas.1100428108.

835   Duvernoy HM, Delon S, Vannson JL. Cortical blood vessels of the human brain. Brain Res Bull. 1981

836   Nov;7(5):519-79.

837   El-Bouri WK. Multi-scale modelling of the microvasculature in the human cerebral cortex. DPhil

838   thesis, University of Oxford, 2017.

839   El-Bouri WK, Payne SJ. Multi-scale homogenization of blood flow in 3-dimensional human cerebral

840   microvascular networks. J Theor Biol. 2015 Sep 7;380:40-7.

841   El-Bouri WK, Payne SJ. A statistical model of the penetrating arterioles and venules in the human

842   cerebral cortex. Microcirculation. 2016 Oct;23(7):580-590. doi: 10.1111/micc.12318.

843   El-Bouri WK, Payne SJ. Investigating the effects of a penetrating vessel occlusion with a multi-scale

844   microvasculature model of the human cerebral cortex. Neuroimage. 2018 Jan 28;172:94-106. doi:

845   10.1016/j.neuroimage.2018.01.049.

846   Fang Q, Sakadzic S, Ruvinskaya L, Devor A, Dale AM, Boas DA. Oxygen advection and diffusion in a

847   three- dimensional vascular anatomical network. Optics Express. 2008;16:17530–17541.

848   Flores J, Alastruey J, Corvera Poiré E. A Novel Analytical Approach to Pulsatile Blood Flow in the

849   Arterial Network. Ann Biomed Eng. 2016 May 2.

850   Formaggia L, Nobile F, Quarteroni A and Veneziani A. Multiscale modelling of the circulatory system:

851   a preliminary analysis. Comput. Vis. Sci. 1999;2:75–83.

852   Gagnon L, Sakadžić S, Lesage F, Musacchia JJ, Lefebvre J, Fang Q, Yücel MA, Evans KC, Mandeville ET,

853   Cohen-Adad J, Polimeni JR, Yaseen MA, Lo EH, Greve DN, Buxton RB, Dale AM, Devor A, Boas DA.

854   Quantifying the microvascular origin of BOLD-fMRI from first principles with two-photon

855   microscopy and an oxygen-sensitive nanoprobe. J Neurosci. 2015 Feb 25;35(8):3663-75. doi:

856   10.1523/JNEUROSCI.3555-14.2015.

857   Gould IG, Linninger AA. Hematocrit distribution and tissue oxygenation in large microcirculatory

858   networks. Microcirculation. 2015 Jan;22(1):1-18. doi: 10.1111/micc.12156.

859   Gould IG, Tsai P, Kleinfeld D, Linninger A. The capillary bed offers the largest hemodynamic

860   resistance to the cortical blood supply. J Cereb Blood Flow Metab. 2017 Jan;37(1):52-68.

861   Guibert R, Fonta C, Plouraboué F. Cerebral blood flow modeling in primate cortex. J Cereb Blood

862   Flow Metab. 2010 Nov;30(11):1860-73. doi: 10.1038/jcbfm.2010.105.

863   Hillman EM, Devor A, Bouchard MB, Dunn AK, Krauss GW, Skoch J, Bacskai BJ, Dale AM, Boas DA.

864   Depth-resolved optical imaging and microscopy of vascular compartment dynamics during

865   somatosensory stimulation. Neuroimage. 2007 Mar;35(1):89-104.

866   Holmes MH. Introduction to Perturbation Methods. Springer. 2013.

867   Kasischke KA, Lambert EM, Panepento B, Sun A, Gelbard HA, Burgess RW, Foster TH, Nedergaard M.

868   Two-photon NADH imaging exposes boundaries of oxygen diffusion in cortical vascular supply

869   regions. Journal of Cerebral Blood Flow and Metabolism. 2011;31:68–81.

870   Kiani MF, Hudetz AG. A semi-empirical model of apparent blood viscosity as a function of vessel

871   diameter and discharge hematocrit. Biorheology. 1991;28(1-2):65-73.

872   Kim JH, Khan R, Thompson JK, Ress D. Model of the transient neurovascular response based on

873   prompt arterial dilation. J Cereb Blood Flow Metab. 2013 Sep;33(9):1429-39. doi:

874   10.1038/jcbfm.2013.90.

875   Kong Y, Zheng Y, Johnston D, Martindale J, Jones M, Billings S, Mayhew J. A model of the dynamic

876   relationship between blood flow and volume changes during brain activation. J Cereb Blood Flow

877   Metab. 2004;24:1382–1392.

878   Langewouters GJ, Wesseling KH, Goedhard WJ. The static elastic properties of 45 human thoracic

879   and 20 abdominal aortas in vitro and the parameters of a new model. J Biomech. 1984;17(6):425-

880   35.

881   Lauwers F, Cassot F, Lauwers-Cances V, Puwanarajah P, Duvernoy H. Morphometry of the human

882   cerebral cortex microcirculation: general characteristics and space-related profiles. Neuroimage.

883   2008 Feb 1;39(3):936-48.

884   Linninger AA, Gould IG, Marinnan T, Hsu CY, Chojecki M, Alaraj A. Cerebral microcirculation and

885   oxygen tension in the human secondary cortex. Ann Biomed Eng. 2013 Nov;41(11):2264-84. doi:

886   10.1007/s10439-013-0828-0. Epub 2013 Jul 11.

887   Lorthois S, Cassot F, Lauwers F. Simulation study of brain blood flow regulation by intra-cortical

888   arterioles in an anatomically accurate large human vascular network: Part I: methodology and

889   baseline flow. Neuroimage. 2011 Jan 15;54(2):1031-42.

890   Lucas C. An anatomical model of the cerebral vasculature and blood flow. DPhil thesis, University of

891   Oxford, 2012.

892   Murray CD. The Physiological Principle of Minimum Work: I. The Vascular System and the Cost of

893   Blood Volume. Proc Natl Acad Sci U S A. 1926 Mar;12(3):207-14.

894   Mut F, Wright S, Ascoli GA, Cebral JR. Morphometric, geographic, and territorial characterization of

895   brain arterial trees. Int J Numer Method Biomed Eng. 2014 Jul;30(7):755-66. doi:

896   10.1002/cnm.2627. Epub 2014 Jan 27.

897   Park CS, Payne SJ. A generalized mathematical framework for estimating the residue function for

898   arbitrary vascular networks. Interface Focus. 2013 Apr 6;3(2):20120078. doi:

899   10.1098/rsfs.2012.0078.

900   Payne, S.J. Methods in the analysis of the effects of gravity and wall thickness in blood flow through

901   vascular systems. In World Scientific Publishing Company themed volume on 'Biomechanical

902   Systems', ed. C.T. Leondes, 2007.

903   Payne SJ. Cerebral blood flow and metabolism: A quantitative approach. World Scientific Publishing.

904   2017.

905   Payne SJ, Lucas C. Oxygen delivery from the cerebral microvasculature to tissue is governed by a

906   single time constant of approximately 6 seconds. Microcirculation, in press.

907   Pedrizzetti G, Perktold K. Cardiovascular Fluid Mechanics. Springer. 2003.

908   Pries AR, Secomb TW. Microvascular blood viscosity in vivo and the endothelial surface layer. Am J

909   Physiol Heart Circ Physiol. 2005 Dec;289(6):H2657-64. Epub 2005 Jul 22.

910   Pries AR, Secomb TW, Gaehtgens P, Gross JF. Blood flow in microvascular networks. Experiments and

911   simulation. Circ Res. 1990 Oct;67(4):826-34.

912   Pries AR, Neuhaus D, Gaehtgens P. Blood viscosity in tube flow: dependence on diameter and

913   hematocrit. Am J Physiol. 1992 Dec;263(6 Pt 2):H1770-8. Review.

914   Pries AR, Secomb TW, Gaehtgens P. Biophysical aspects of blood flow in the microvasculature.

915   Cardiovasc Res. 1996 Oct;32(4):654-67. Review.

916   Reichold J, Stampanoni M, Lena Keller A, Buck A, Jenny P, Weber B. Vascular graph model to

917   simulate the cerebral blood flow in realistic vascular networks. J Cereb Blood Flow Metab. 2009

918   Aug;29(8):1429-43.

919   Ress D, Thompson JK, Rokers B, Khan RK, Huk AC. A model for transient oxygen delivery in cerebral

920   cortex. Front Neuroenergetics. 2009 Jun 29;1:3. doi: 10.3389/neuro.14.003.2009. eCollection

921   2009.

922   Safaeian N, Sellier M, David T. A computational model of hemodynamic parameters in cortical

923   capillary networks. J Theor Biol. 2011;271(1):145-156.

924   Schmid F, Tsai PS, Kleinfeld D, Jenny P, Weber B. Depth-dependent flow and pressure characteristics

925   in cortical microvascular networks. PLoS Comput Biol. 2017 Feb 14;13(2):e1005392. doi:

926   10.1371/journal.pcbi.1005392. eCollection 2017 Feb.

927   Shipley RJ, Chapman SJ. Multiscale modeling of fluid and drug transport in vascular tumors. Bull

928   Meth Biol. 2010;72:1464-91.

929   Stergiopoulos N, Young DF, Rogge TR. Computer simulation of arterial flow with applications to

930   arterial and aortic stenoses. J.Biomech. 1992;25:1477–1488.

931   Su SW, Catherall M, Payne S. The influence of network structure on the transport of blood in the

932   human cerebral microvasculature. Microcirculation. 2012;19:175–187.

933   Tsai PS, Kaufhold JP, Blinder P, Friedman B, Drew PJ, Karten HJ, Lyden PD, Kleinfeld D. Correlations of

934   neuronal and microvascular densities in murine cortex revealed by direct counting and

935   colocalization of nuclei and vessels. Journal of Neuroscience. 2009;29:14553–14570.

936 Unekawa M, Tomita M, Tomita Y, Toriumi H, Miyaki K, Suzuki N. RBC velocities in single capillaries of

937   mouse and rat brains are the same, despite 10-fold difference in body size. Brain Res. 2010 Mar

938   12;1320:69-73. doi: 10.1016/j.brainres.2010.01.032. Epub 2010 Jan 18.

939 Vazquez AL, Masamoto K, Fukuda M, Kim SG. Cerebral oxygen delivery and consumption during

940   evoked neural activity. Front Neuroenergetics. 2010 Jun 18;2:11. doi: 10.3389/fnene.2010.00011.

941 Weber B, Keller AL, Reichold J, Logothetis NK. The microvascular system of the striate and

942   extrastriate visual cortex of the macaque. Cerebral Cortex. 2008;18:2318–2330.

943 Womersley, JR. Method for the calculation of velocity, rate of flow and viscous drag in arteries when

944   the pressure gradient is known. J Physiol. 1955 Mar 28;127(3):553-63.

945 Zheng Y, Mayhew J. A time-invariant visco-elastic windkessel model relating blood flow and blood

946   volume. Neuroimage. 2009;47:1371–1380.